Capacitive Transducers With Curved Electrodes

Robert B. McIntosh, *Senior Member, IEEE*, Philip E. Mauger, and Steven R. Patterson

***Abstract*—The design, performance, and potential applications are described for capacitive transducers with curved electrodes. A curved electrode governs the deflection of a compliant electrode under applied stress. A dielectric film on one electrode provides a variable region of fixed electrode spacing. The sensitivity and linear dynamic range of the transducers are higher and wider than devices with parallel electrodes. An electrical advantage is obtained from the permittivity of the dielectric film and a mechanical advantage from its thinness. Transducers have been constructed with silicon diaphragms that bend and polymer membranes that stretch in response to uniform pressure. The silicon sensors measured dynamic pressure changes over a linear range of 125 dB. An 885% change in capacitance was obtained for a sensor with a thin silicon diaphragm. Sensors with polycarbonate membranes demonstrated the ability of a low-cost transducer to measure pressure, fluid flow, displacement, and tilt. An active capacitive bridge circuit was developed to linearly measure capacitance changes up to 1000% and to control electrostatic actuators by force-balanced feedback. Methods and materials to construct microscale transducers are discussed along with the performance limitations of electrostatic actuation.**

***Index Terms*—Capacitive transducer, curved electrode, electret transducer, electrostatic actuator, force-balanced feedback, null-balanced bridge (NBB), ultrasound transducer.**

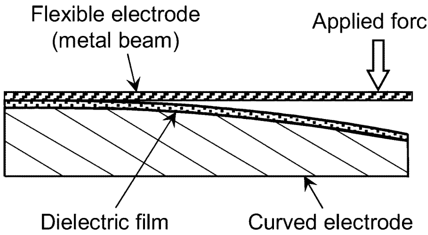

Fig. 1. Capacitive displacement transducer of Carter *et al.*, 1945.

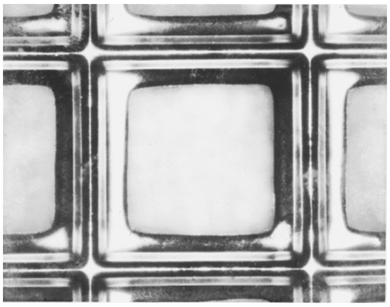

Fig. 2. Portion of the micromachined silicon electrode structure of a microphone with curved support ribs.

I. BACKGROUND

THE transducers described in this paper have a compliant electrode, a thin-film dielectric, and a rigid electrode with a predetermined surface contour. The major portion of a change in capacitance arises from a change in effective electrode area.

A sensor with a curved electrode developed during WWII at the Royal Aircraft Establishment, U.K., to measure displacement and strain was described by Carter *et al.* in 1945 [1]. This sensor had a compliant beam electrode that deformed in an arc around a cylindrical electrode. This transducer is conceptually shown in Fig. 1. A majority of its capacitance is caused by electric field coupling across a thin, dielectric layer in the region of electrode contact. In 1959, Frank calculated the extraordinary resolution of this transducer in an example used to illustrate the operation of a DeSauty bridge [2].

Slavin *et al.* in 1976 and Young *et al.* in 2004 describe pressure sensors with compliant diaphragms that collapse against a planar electrode [3], [4]. A preload pressure establishes a point of initial electrode contact, after which the area of electrode contact increases with pressure. For these designs, it is difficult to anticipate or control the free-form deflection of the diaphragm. Basarab-Horwath and Jones recognized the advantage of constructing a similar capacitive transducer with a dielectric of high permittivity, i.e., tantalum pentoxide [5].

In 1992, microphones were constructed by suspending 1.5-μm-thick, silicon diaphragms over a rigid electrode structure of support ribs with rounded top edges. They were fabricated by P. Mauger (author) and measured by V. Nedzelnitsky at the U.S. National Institute of Standards and Technology [6]. The transducer concept was suggested to the authors by B. Block [7]. A 4-mm-square diaphragm was suspended over an array of nine 1-mm-square elements micromachined from silicon, as shown in Fig. 2. Thermally grown oxide on the structure served as the fixed dielectric.

The acoustic sensitivity of the sensor (-38 dB re 1 V/Pa) was found to be equivalent to a B&K 4133, 12.7-mm (1/2 in) diameter microphone. However, this value was severely limited by the small radius of the support ribs and active electrode area. This experience led to the development of transducers with the electrode structures described here and in [8].

The capacitance structure of Fig. 1 is often used to construct electrostatic actuators. One example is the surface micromachined cantilever beam actuator described by Legtenberg *et al.* [9]. However, the force developed by this and other actuators is limited by the accumulation and trapping of charge in thin-film

---

Manuscript received December 3, 2004; revised April 5, 2005. This work was supported in part by the U.S. Department of Navy under Contracts N0024-96-C-4221, N0024-97-C-4157, and N61331-98-C-0039 and in part by by the U.S. Department of Air Force under Contract F33615-96-C5460. The associate editor coordinating the review of this paper and approving it for publication was Dr. Ai-Qun Liu.

R. B. McIntosh, Consultant, Williamgburg, VA 23185 USA (e-mail: horizontechnology@cox.net).

P. E. Mauger is with Nanostructures, Inc., Santa Clara, CA 95051 USA (e-mail: pmauger@nanostructures.com).

S. R. Patterson University of North Carolina at Charlotte, Charlotte, NC 28223 USA.

Digital Object Identifier 10.1109/JSEN.2005.854137

dielectrics. The field strength in the dielectric must remain well below the dielectric strength of the material.

More applications might exist for actuators if their capacitance was sensed to control electrode displacement by force-balanced feedback. This can be accomplished at one capacitor electrode when its cooperating electrode is grounded [10].

II. TRANSDUCER DESIGN

A. Introduction

Transducers with curved electrodes were constructed with silicon diaphragms that bend and polymer membranes that stretch in response to applied stress. The contour of the rigid electrode was selected to provide a linear capacitive response over a wide dynamic range. This condition exists when the annular area of fixed electrode spacing increases linearly with uniform applied pressure.

The construction of a simple pressure sensor is shown in Fig. 3. A radially tensioned and metallized polycarbonate (PC) membrane is thermally bonded to a PC substrate. The rigid electrode comprises a thin metal film deposited over a curved contour formed in the substrate. The full-scale range of the device is determined by the tension of the membrane and the depth of the contour at the center of the rigid electrode.

A sectional view of an underwater pressure sensor with a silicon diaphragm is shown in Fig. 4. The diaphragm is anodically bonded to a borosilicate glass substrate in which a curved contour is formed. The specific form of the contour is selected to provide a linear capacitance response over a wide dynamic range. For this design, the capacitor dielectric film is deposited on the bottom of the conducting silicon diaphragm.

B. Capacitance Values

The total capacitance C of sensors with curved electrodes has three components: $C_C + C_G + C_0$. Capacitance C_C is due to electric field coupling across the thin dielectric, C_G is a smaller variable capacitance between the unsupported diaphragm and rigid electrode, and C_0 is a passive component due to fringing fields around the bonded edge of the electrodes.

A linear model of a capacitive transducer with a contoured electrode is shown in Fig. 5. The contour is a shallow conical depression with a center-point depth $s = s_0 + s_d$. A piston-type displacement s_d of the diaphragm is assumed for a uniform quiescent pressure P_0. The shape of the unsupported area of the diaphragm does not significantly alter results of interest. A small angle of electrode approach α is obtained by selecting a spacing $s \ll R$, where R is the radius of the rigid electrode. Capacitance C_C in the annular region of contact $(r_0 \leq r \leq R)$ is

$$C_C \approx \frac{\varepsilon_a \pi}{t_d}\left(R^2 - r_0^2\right) \tag{1}$$

where ε_a equals the permittivity of the fixed dielectric layer, r_0 the radius of the boundary of electrode contact, and t_d the thickness of the dielectric layer.

The capacitance C_G in the region of the electrode gap is found in Appendix-A to be

$$C_G \approx C_P\left[\ln(K_p + 1) - 1\right] \tag{2}$$

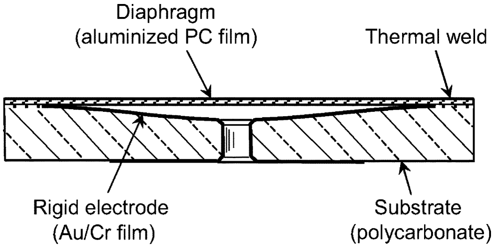

Fig. 3. PC pressure sensor with pretensioned membrane.

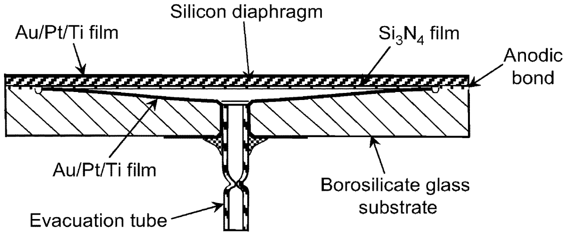

Fig. 4. Pressure sensor with a silicon diaphragm. The vertical scale is exaggerated to show construction details.

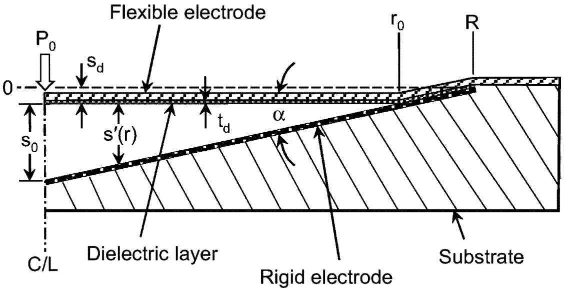

Fig. 5. Half-section of a capacitor with a conical electrode.

where C_P is the static value of a parallel-plate capacitor with radius r_0 and electrode spacing $s_0 = s - s_d$. The term K_p is a performance factor identified below in (6).

C. Capacitive Sensitivity

A substantial portion of the capacitance displacement sensitivity S_A of a sensor with a quiescent diaphragm displacement s_d, contact radius r_0, and center-point electrode spacing s_0 can be found by differentiating (1)

$$S_A = \frac{dC_C}{ds_0} = \frac{dC_C}{dr_0}\frac{dr_0}{ds_0} = \frac{-2\varepsilon_a \pi r_0}{t_d}\frac{dr_0}{ds_0}. \tag{3}$$

Referring to Fig. 5, the slope of the rigid electrode $dr_0/ds_0 = r_0/(s - s_d) = r_0/s_0$. Equation (3) now can be expressed as

$$S_A = -\frac{2\varepsilon_a \pi r_0^2}{t_d s_0}. \tag{4}$$

This result is reasonable: S_A increases with electrode area and with the permittivity and thinness of the dielectric film.

By contrast, a parallel-plate capacitor C_p with electrodes of radius r_0 and spacing s_0 has a capacitance value of $\varepsilon\pi r_0^2/s_0$, where ε is the permittivity of dry air, a value close to ε_0 of free space. Its displacement sensitivity is

$$S_P = \frac{dC_P}{ds_0} = -\frac{\varepsilon_0 \pi r_0^2}{s_0^2}. \tag{5}$$

From (4) and (5), the ratio S_A/S_P is

$$\frac{S_A}{S_P} = 2\frac{\varepsilon_a s_0}{\varepsilon_0 t_d} = 2K_p. \tag{6}$$

K_p is a figure-of-merit that allows the performance of transducers with curved electrodes to be compared to sensors and actuators with parallel electrodes. It is the product of a relative electrical advantage $\varepsilon_a/\varepsilon_o$ and a mechanical advantage s_0/t_d. Practical design values of $2K_p$ range between 200 to over 10 000. High values of K_p are obtained with thin dielectrics, but film thickness is limited by the type and method of deposition and, ultimately, by the dielectric strength of the material.

D. Electrostatic Force

When a voltage V is applied to a capacitor with a curved electrode, it exerts an electrostatic force F_A on its electrodes. This force can be determined from the energy stored on the capacitor, $W_e = CV^2/2$. Substituting (4) for dC_C/ds_0, F_A can be expressed as

$$F_A = \frac{dW_e}{ds_0} = \frac{1}{2}\frac{dC_C}{ds_0}V^2 = -\frac{\varepsilon_a \pi r_0^2 V^2}{t_d s_0}. \tag{7}$$

By contrast from (5), the force F_P arising from a voltage V across parallel electrodes of radius r_0 and spacing s_0 is

$$F_P = -\frac{\varepsilon_0 \pi r_0^2 V^2}{2s_0^2}. \tag{8}$$

From (7) and (8)

$$\frac{F_A}{F_P} = 2\frac{\varepsilon_a s_0}{\varepsilon_0 t_d} = 2K_p. \tag{9}$$

The majority of force F_A acts on the annular region of electrode contact. For actuators with membrane electrodes, the center of the membrane remains flat because of a piston-type displacement. This characteristic suggests applications for optical beam displacement, etalons and other tuned cavities.

The high force exerted by an actuator with a curved electrode can be traded off to allow microelectromechanical (MEM) devices to operate at low voltages, e.g., micromirrors for tunable surface-emitting lasers and magnetooptical disk drives. [11], [12]. The high sensitivity and force of sensors and actuators with contoured electrodes allow them to operate with stiffer electrodes and etch-released structures to reduce Brownian motion.

E. Electrode Contour

The shape of a rigid electrode required to provide a linear response over a wide dynamic range depends upon the reaction stresses that develop within the compliant electrode. The deflection of a stiff diaphragm is primarily determined by bending stresses, while that of a membrane is established by tension. The following constraint applies to capacitors with circular electrodes when a majority of the capacitance is determined by an annular area of electrode contact:

$$R^2 - r^2(p) = \xi p \tag{10}$$

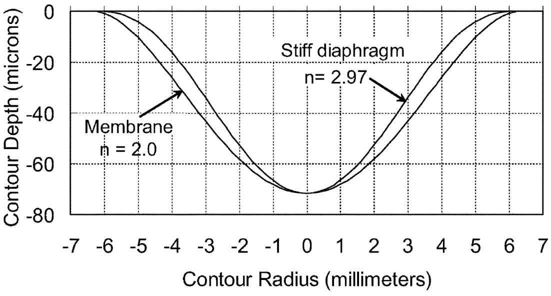

Fig. 6. Electrode contours of a pressure sensor with a stiff diaphragm and a tensioned membrane.

where ξ is a constant and p uniform pressure. When this condition is satisfied, the pressure sensitivity dC/dp of the capacitor equals ξ, within the tolerances of fabrication.

The general form

$$z(r) = K\left(1 - \frac{r^2}{R^2}\right)^n \tag{11}$$

provides a good approximation for a variety of designs. It is shown in Appendix-B that exponent $n = 2.0$ in (11) for a sensor with a pretensioned membrane under uniform pressure. Changes in tension caused by small membrane displacements are negligible compared to the initial value of assembled tension. An electrode contour derived from this form is shown in Fig. 6. It is significant that it is independent of membrane tension T and full-scale pressure. Errors in T affect a calibration constant, not device linearity. It is of interest to note that this form is the same as the generatrix of a circular, edge-clamped plate subjected to uniform pressure.

A more complex analysis was performed to calculate the contour for sensors with stiff silicon diaphragms. It assumed the deformation of the diaphragm is small compared to other dimensions of the problem. This allowed linear superposition to be used to construct a solution as a combination of one resulting from uniform pressure distributed over a disk freely supported at the edges and that of a disk with only a uniform moment couple at the edges.

When bending stresses dominate diaphragm deflection, exponent n of (11) was found to be 2.97. The form is a doubly curved surface with a characteristic inflection, shown in Fig. 6. It is independent of the diameter and thickness of the diaphragm. However, this analysis is too lengthy to be included herein. The contours can also be modified to compensate for nonlinear stresses, electronics, and other system effects.

The precise shape of the rigid electrode is not critical for microphones, accelerometers, and ultrasonic transducers that have small membrane displacements around a mechanically fixed or electrically biased operating point. The small-signal sensitivity for these devices is determined by the local slope of the contour at the quiescent point of electrode contact. The exact shape of the dish is important for absolute pressure sensors that cannot be compensated by stored calibration data.

F. Dielectric Films

The sensitivity of the PC sensor of Fig. 3 can be increased by depositing a thin dielectric layer over the rigid electrode structure and then bonding the metallized side of the membrane to the substrate. Candidate dielectrics include CVD parylene (polyparaxylene), spin-coated PVDF (polyvinylidene fluoride), or Teflon AF. Parylene-N is an attractive material because of its high dielectric strength, 275 V/μm, and low dielectric dissipation factor (loss tangent) of 0.0002, important parameters for acoustic projectors [13]. An additional advantage is it is deposited by CVD at room temperature to form conformal, pinhole-free, sub-micron thick films. The charging of parylene films in air and vacuum are reported in [14].

Silicon dioxide, nitride, and oxynitride films were used as the dielectric for pressure sensors with silicon diaphragms. These films, deposited by LPCVD or PECVD, were thermally annealed to increase their mechanical strength to minimize possibile mechanical stress-induced leakage currents. Silicon nitride has the highest dielectric constant, but this advantage is compromised by a higher density of charge trapping sites in the bulk material and at the film interfaces, which limits its potential use with MEMS electrostatic actuators.

Recent advances in the development of high-k gate dielectrics (e.g., stoichiometric nanocrystalline hafnium-based films) have the potential to enhance the performance of low-voltage sensors and actuators. The thinness and electron mobility of these promising materials can be relaxed for the applications identified below in Section VII.

G. Variable Gap Capacitance

The capacitance sensitivity S_A from (4) assumed the contact capacitance C_C of the transducer is large compared to its gap capacitance C_G. The extent to which this assumption is valid can be estimated using the data of Table I. Here, $K_p = \varepsilon_r s_0/t_d$, where $\varepsilon_r = \varepsilon_a/\varepsilon_o$ is the relative permittivity of the dielectric. The values for K_p are for an electrode with a radius, $R =$ 6.2 mm, and a center depth $s_0 = 72$ μm.

The total capacitance C of a transducer equals the sum of its contact capacitance C_C, gap capacitance C_G, and passive capacitance C_0. Values for C_0 are estimated by subtracting calculated values of C_G obtained from (2) from C without an applied stress. The theoretical value of $K_p = 4300$ is for a sensor with a silicon diaphragm with a 0.1-μm-thick SiN film. The value of K_p is about 1000 for high pressure silicon sensors with a thick SiN/SiO$_2$ dielectric. This value is reduced by the surface texture of the substrate which increases the effective thickness t_d of the dielectric while lowering its permittivity.

Table I shows that K_p is only 72 for a sensor with a 3-μm-thick PC membrane when the membrane serves as the fixed dielectric. This value of K_p can be increased to about 380 when the bottom of the PC diaphragm is metallized and the electrode structure is covered with a 0.5-μm-thick film of parylene. A value of K_p is also given for a sensor with a tantalum pentoxide film to illustrate the advantage of a high permittivity dielectric.

The ratio of contact capacitance C_C to total capacitance C as a percentage of electrode contact area, $A = \pi(R^2 - r_0^2)$, is plotted in Fig. 7. Curves of C_C/C indicate C_G contributes to C at small diaphragm displacements. This contribution is less for sensors that are mechanically or electrically preloaded.

TABLE I
TYPICAL DESIGN AND MATERIAL PARAMETERS

C_0 (pF)	ε_r	t_d (μm)	K_p	Dielectric
500	22	0.2	7900	T$_2$O$_5$; annealed
300	6	0.1	4300	SiN
155	3.5	0.25	1000	SiN/SiO$_2$
50	2.65	0.5	380	Parylene-N
10	3	3	72	Polycarbonate

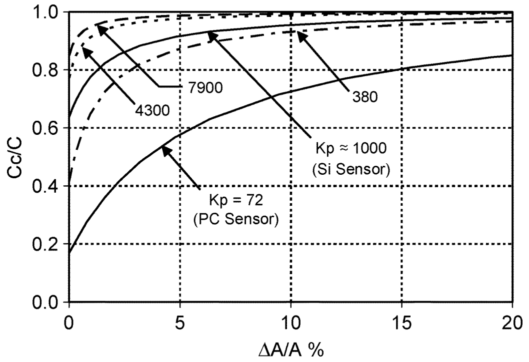

Fig. 7. Ratio of contact capacitance C_C to total capacitance C as a percentage of electrode contact area for different values of K_p.

H. Physical Noise Limits

Two fundamental sources of noise in capacitive transducers arise from the thermal variations of charge and from the Brownian motion of diaphragms and suspended structures. For a system with a single capacitor C, the total mean-square thermal noise voltage Δv^2 over the bandwidth of the system is kT/C, where k is Boltzmann's constant and T is absolute temperature. If bandwidth is determined by a resistor R, then the noise bandwidth $\Delta f = \pi/2(1/2\pi RC)$ and Δv^2 becomes the familiar expression for Johnson noise, $\Delta v^2 = 4kTR\Delta f$. Compared to conventional capacitors of comparable size, capacitors with curved electrodes have higher capacitance values under all conditions of loading which provides a signal-to-noise advantage, in addition to S/N enhancement by the factor $2K_p$.

Brownian noise arises from forces coupled to microstructure from the kinetic energy of molecules in a surrounding fluid. The Brownian noise of ultrasensitive pressure sensors are described by Chau and Wise in [15] and for accelerometers by Gabrielson in [16]. This noise is generally low compared to other sources of noise for devices with small, low-stress diaphragms at frequencies below resonances. Although this noise is expected to be more significant for more sensitive transducers with curved electrodes, an estimate of its value is design and application specific, a subject for future research.

Noise is also generated by a variety of intrinsic and extrinsic hysteretic damping mechanisms. One example is noise associated with energy dissipation in a crystalline diaphragm due to impurities, grain boundaries, and dislocations.

A unique damping mechanism in capacitors with a curved electrode arises from interfacial stick-slip between the capacitor electrodes. For smooth surfaces, damping losses occur due to a random variation of adhesion energy between the extension and contraction of the area of electrode contact. At low frequencies, this noise can be reduced by electrostatically induced vibration (dithering) generated by the periodic excitation voltage of detection circuitry, as is the case for electronics described below.

III. TRANSDUCER ELECTRONICS

A. Null-Balanced Capacitance Bridge

A new capacitance measurement circuit was developed to accommodate the very large capacitance changes of transducers with curved electrodes, when one electrode is grounded [17]. The circuit is an active, null-balanced bridge (NBB) that detects a change between a variable capacitor C_S and a reference capacitor C_R. The bridge concept is shown in Fig. 8.

The bridge excitation voltage $v_E(t)$ is a train of precision pulses of amplitude V_E that periodically charge C_R and C_S through an integrated pair of Schottky diodes or FET switches. The voltage V_E on C_R is then discharged by a constant current source i_0 from time T/5 until the arrival of the next pulse at time T, as shown by waveform $v^+(t)$ in Fig. 9. A voltage-controlled current source (VCCS) simultaneously discharges C_S by a current i during the same period of time.

When a pressure ΔP is applied to a sensor, its capacitance C_S increases by ΔC, which increases the running average of periodic voltage $v^-(t)$. A discharge current $i > i_0$ is now required to discharge C_S to V_1 by time T. The bridge outputs, $v^+(t)$ and $v^-(t)$, are connected to the circuit of Fig. 10 that functions as an inverting differential VCCS. Two low-pass filters (resistors and capacitors: R_1, C_1, and R_2, C_2) provide running averages of $v^+(t)$ and $v^-(t)$ to the inputs of an operational amplifier. The amplifier output sinks a current i that is conveyed through transistor T_1 to force by feedback $v^-(t) = v^+(t)$. When the quiescent capacitance of $C_S = C$, and $C = C_R$, the null condition requires

$$\frac{i_0}{C_R} = \frac{i_0 + \Delta i_0}{C_S + \Delta C_C} \quad \text{and} \quad \Delta i_0 = i_0 \frac{\Delta C}{C}. \tag{12}$$

The amplifier output voltage, $V = V_0 + \Delta V_0$, is developed by current $i = i_0 + \Delta i_0$ through R_f, whereby $\Delta V = i_0 R_f \Delta C / C$. The circuit of Fig. 10 functions as a current servo with an open-loop gain of 140 dB at dc with an AD707 amplifier. A small feedback capacitor C_f ensures high-frequency stability.

The bridge excitation pulses, with a 20% duty cycle, are generated by a micromachined quartz, tuning-fork oscillator, and a 74HCT390 counter connected in a bi-quinary counting mode. The bridge and VCCS were operated together at frequencies between 10 KHz and 1 MHz. The source impedance of the bridge is determined by its excitation frequency and the reactances of C_S and C_R. The amplitude of the pulses is established by a buffered 10-V reference. A 2.5-V reference can be used for micropower applications.

B. Additional Advantages of NBB

A major advantage of a NBB is that all fixed and parasitic capacitances are initially charged together to V_E. A differential change in $v^+(t)$ and $v^-(t)$ does not occur until after the voltage starts to discharge at time T/5.

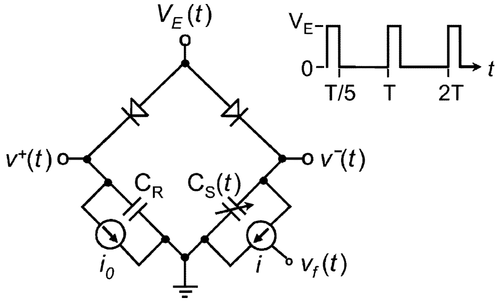

Fig. 8. Active capacitance bridge nulled by current feedback.

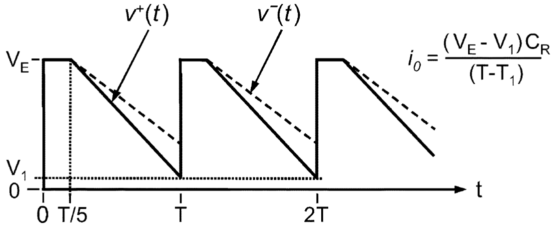

Fig. 9. NBB waveforms.

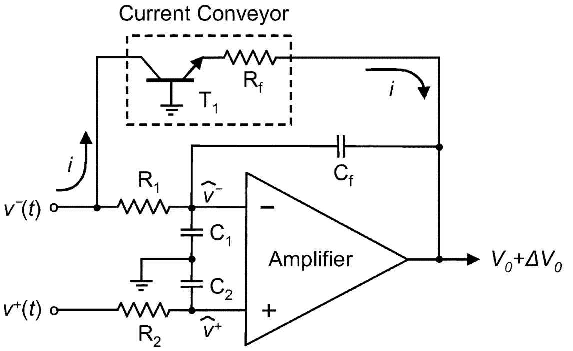

Fig. 10. Differential voltage-controlled current source.

Another advantage is that large passive and active capacitances of a capacitor with electrodes in partial contact decrease the impedance and noise of the bridge, but this requires more power to be supplied by the excitation circuitry.

The excitation voltage applies a time varying electrostatic force to the compliant electrode. This has the potential to reduce mechanical stiction for MEMS sensors and actuators. The resulting microscale vibration continuously reseats the electrode as it collapses and relaxes across the surface of the rigid electrode. However, high-frequency bridge excitation is required for cavity-tuned optical and RF MEMS.

C. Other Circuit Arrangements

A simpler circuit described in [17], with near-optimal performance, was constructed by replacing the current sources in the NBB of Fig. 8 with resistors and by deleting transistor T_1 in the circuit of Fig. 10. The parallel resistors exponentially discharge C_R and C_S, and $v^+(t)$ and $v^-(t)$ become trains of exponentially decaying pulses. Fig. 11 is a plot of the output voltage versus capacitance change for this circuit arrangement.

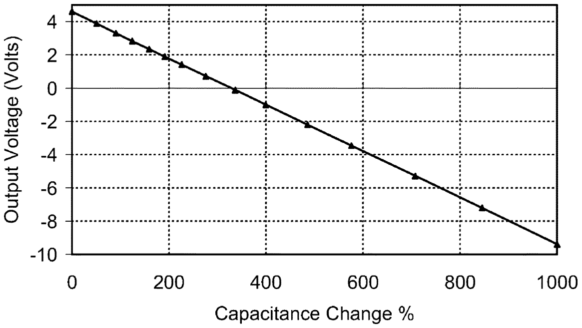

Fig. 11. Linear response of capacitance measurement electronics.

A NBB can be used with all type of capacitive transducers for precision measurements at dc and frequencies below the excitation frequency of the bridge. Also, a difference between two capacitors of a differential transducer, with a common compliant or movable electrode, can be detected when capacitor C_R is replaced by a second variable capacitor in the NBB.

The advantage of current feedback can be realized with a half-bridge circuit when $v^+(t)$ in Fig. 10 is provided by a fixed reference voltage. This voltage can be varied to control the electrode displacement of an actuator.

D. Minimum Detectable Pressure Change

At frequencies below about 10 Hz, the minimum detectable pressure change that can be resolved by a capacitive sensor is limited by 1/f noise and avalanche noise of a buried zener diode in a low-noise voltage reference. The rms voltage e_n for 1/f noise between frequencies f_1 and f_2 can be expressed as

$$e_n = K\sqrt{\int_{f_1}^{f_2} \frac{df}{f}} = K\sqrt{\ln\frac{f_2}{f_1}} \tag{13}$$

where K is the noise spectral density $(\mathrm{nV}/\sqrt{\mathrm{Hz}})$ at 1.0 Hz [18].

As an example, (13) can be used to determine the typical 1/f noise corner-frequency of an AD587, 10-V reference. It is located at about 10 Hz based upon a specified nominal noise spectral density of 100 $\mathrm{nV}/\sqrt{\mathrm{Hz}}$ at 100 Hz and 4-$\mu\mathrm{V}_{\mathrm{p-p}}$ noise over a bandwidth of 0.1–10 Hz. Equation (13) can be used again to calculate the lower bound of the peak-to-peak noise floor of a sensor over a specified noise bandwidth.

The noise of voltage references exceed the values obtained from (13) by 3–6 dB, because of unspecified avalanche noise. Its level can inferred by observing the amplified voltage difference between two references. This method can also be used iteratively to select lower noise devices.

In principle, the dynamic range of the active bridge can be extended by changing the value of the fixed reference capacitor at fixed scale increments. For this circuit arrangement, the dynamic range of a transducer with a low stress membrane may be found to be limited by noise associated with hysteretic losses of electrode contact motion.

For dc measurements, the NBB has the same limitations as those of precision dc-coupled electronics: the thermal sensitivity of circuit elements and thermally induced offset voltages of junctions of dissimilar lead and conducting materials.

Fig. 12. Pressure sensors with silicon diaphragms (right) and polycarbonate membranes (left). The sensors are 19 mm in diameter.

IV. FABRICATION

A. Pressure Sensors With Silicon Diaphragms

Sensors with the construction of Fig. 4 were fabricated with silicon diaphragms, 470-, 100-, and 25-μm thick. The sensors at the left in Fig. 12 have 0.47-mm-thick diaphragms for ocean-bottom pressure sensing.

The diaphragms were fabricated from double-side polished, $\langle 100\rangle$ p-type silicon wafers with a resistivity of 1–10 Ωcm. The wafers were etched in an aqueous solution of KOH to the desired thickness. During the etch back of the thinner 25-μm, diaphragms, a 4.5-mm-wide hexagonal hub (inertial mass) was formed in the center of the diaphragm using a circular oxide mask. These diaphragms were used to construct displacement sensors, accelerometers and tilt sensors.

A 1600-Å-thick film of oxide was thermally grown on the thinned wafers to form a first dielectric layer. Next, a 1700-Å-thick layer of SiN was deposited by PECVD at 800 °C, followed by a high-temperature anneal in air at 900 °C to complete the fixed dielectric layer of the capacitor. A double-layer film was used to avoid any mechanical stress-induced leakage current because of the low-noise floor of the detection electronics.

The dielectric was removed from the top of the wafer to be metallized. It also was removed from the bottom of the wafer at and outside each anodic bond site. This reduced the temperature and voltage required to form reliable bonds to 360 °C and 350 V. The wafer was then cut into hexagonal diaphragms (see Fig. 12 bottom left) by a computer-controlled, K&S-7500, Wafer Dicing Saw.

Contoured substrates (19 mm in diameter) were fabricated from Pyrex 7740 glass with the shape shown in Fig. 6 for $n = 2.97$. A chamfered, 1.6-mm-diameter hole with polished side walls was formed through the center of the substrate. The through-hole provided an evacuation port and a via to electrically connect the contoured electrode. After anodic bonding of the diaphragm to the substrate, a gold-plated, copper pinch-off tube was inserted into the hole and soldered in place at a final step of assembly, as shown in Fig. 12, top left.

Three sputter metal depositions were used to fabricate the sensors. The metal film comprised 2000 Å of Au deposited over

1000 Å of Pt and a 750-Å adhesion baselayer of Ti. The intermediate Pt layer prevented Au from diffusing into, or alloying with, the baselayer at the temperature of anodic bonding. Referring to Fig. 4, a first deposition was applied through a circular mask to form the contoured electrode and to deposit metal on the sidewall of the substrate through hole.

Metal was then deposited on the bottom and outside edge of the substrate and again on the sidewall of the through hole. The bottom-side metal was patterned to form a solder pad around the hole and an electrical contact pad. After anodic bonding of the diaphragm to the substrate, metal was deposited over the diaphragm and again on the sidewalls of the assembly to make an electrical connection to the contact pad on the bottom surface of the substrate.

B. Ductile-Mode Grinding of Glass Substrates

A simple, template-tracing grinding machine was constructed to contour the glass substrates to a near-optical quality form. A 50–0.5-cm lever arm was used to trace an electrodischarge machined template with a 100:1 depth enhancement. The 0.8-mm radius of the tracing stylus matched the cutting radius at the tapered edge of the grinding wheel.

Custom 3.8-cm diameter grinding wheels were fabricated with triply screened, coarse, 80-grit SiC abrasive particles bonded in a hard rubber matrix. The large abrasive particles provided multiple, single-point cutting edges. Only the cutting edges of the particles wore during grinding which were restored when the wheel was trued with a concave tool. The tool was a pulley with a groove in which polycrystalline diamond was captured in an electroplated metal matrix. The as-ground contour of several substrates was measured using a Taylor–Hobson Talysurf with a 2-μm-radius diamond stylus.

The texture of the contoured glass surface had the characteristics of ductile-mode machining: a nested set of irregular concentric microgrooves with smooth ridges and sidewalls. The bottom of the grooves exhibited brittle fracture damage at locations where grinding wheel vibration caused the cutting edge of a SiN grain to drop below the plastic zone of the glass.

Although the brittle fracture could have been reduced by constructing a stiffer machine with air bearing workpiece and high-speed grinding spindles, the silicon diaphragm only mechanically contacts the contour defined by the ridges. The substrates were etched in buffered HF to round the peaks of the ridges and to dislocate loose material. The ductile depth of Pyrex 7740 glass was found to be about 0.25 μm from scans made with a Tencor, Alpha-Step 2000 Profilometer.

Sensors with 0.47-mm-thick silicon diaphragms were fabricated for an ocean-bottom pressure sensor (OBPS) shown in Fig. 13. An ac-coupled output of the sensor is used to detect sub-Hertz Bernoulli velocity fields of ships. Tide and seiche frequencies were removed by high-pass filtering. A second output provided a dc voltage used to determine ocean depth.

C. Sensors With PC Membranes

The contoured substrates of the sensors shown at the right in Fig. 12 were fabricated from optically clear PC. A 3.18-mm-diameter hole in the substrate provided a port for pressure equalization. Metal was deposited on the sidewalls of the hole to electrically connect the contoured electrode to a contact pad on the bottom surface of the substrate.

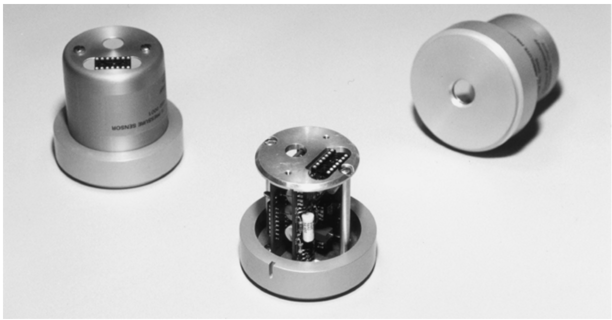

Fig. 13. Ocean-bottom pressure sensors.

For expediency, the template-tracing grinding machine was converted to a single-point diamond turning tool to contour PC substrates. The electrode shape was machined over the face of rod stock to avoid chuck-induced strain before the substrate was parted to its required thickness.

Hot embossing is a preferred production method to form smooth, shallow contours in thermoplastic substrates for meso- and microscale transducers. A heated master is used to transfer the form to a heated substrate, preferable in vacuum. Hot embossing and nano-imprinting technology and tools are commercially available for MEMS production, e.g., [19].

The compliant electrode was 3- or 6-μm-thick PC foil of the type used to manufacture capacitors: a bi-axially formed film on which aluminum is vapor deposited. The foil was first adhered to a stainless-steel support ring and then a second smaller ring was used to tension the foil by the method used to construct pellicles and electret microphones. A heated annular tool mounted on an arbor press was used to weld the foil to the substrate. In production, laser welding may be preferred to bond polymer membranes. It produces a smooth, narrow weld line that minimizes a stress affected zone. Welds can be formed with many thermoplastics, including polyethylene terephthalate (PET) membranes to PETG substrates. PETG is a gycol-modifed, amorphous form of PET.

Bayer AG recently discontinued manufacturing PC film. Bi-axially orientated polyphenylene-sulphide (PPS) and PET films are attractive alternatives [20]. PET (Mylar) foil is commonly used to manufacture electret microphones.

V. TEST METHODS

A. Silicon Pressure Sensors

A Psi-Tronix, PC-10K pressure calibrator was used to measure the static pressure response of silicon sensors and to calibrate the depth channel of the OBPS. The calibrator is shown with a face-sealed OBPS in Fig. 14. Hydraulically developed pressure was monitored with a digital pressure gauge with a NIST traceable, full-scale accuracy of ±0.1%.

The span of the ac output was set at 4.98 kPa (20-in water column). Small-signal gain was measured over an absolute pressure range of 0 to 1.8 MPa at the former, Naval Surface Warfare Center Laboratory, White Oak, MD.

Fig. 14. Setup for static pressure calibration.

The OBPS systems were filled with fine glass beads to assist their survival to high levels of shock and vibration. Two units were exposed to 4000-g sinusoidal shock waves along two axes, before and after a 2-h cold soak at -54 °C. Individual units were also exposed ten times to an over-pressure of 6.9 MPa (1000) psi. No measurable change in sensor performance or noise was observed after these tests.

B. PC Pressure Sensors

The pressure response of the PC sensors was measured in the O-ring sealed test fixture shown at the left of Fig. 15. Pressure was applied to the fixture through flexible tubing attached to a glass syringe. It was measured using Airflow Development, Ltd. monometers: Model 504 (1-in WC full-scale) or Model SJ-12 (12-in WC full-scale). Capacitance was measured with a Stanford Research, Model SR715, LCR meter on a scale having a specified accuracy of 0.2%.

The housing on the right of Fig. 15 was used to measure differential pressure to determine fluid flow rates. The front and back surfaces of a PC sensor, with a 6-μm-thick membrane, were exposed to differential line pressures. A porous, HDPE plug (25-μm porosity) was inserted in the hole of the substrate to provide an over-pressure stop. Sensors with a full-scale pressure range of 0.25 Pa (1-in WC) were exposed to pressure-line faults of 3.4 MPa (500 psi) which caused the plug to compress and emboss a shallow, 3.18-mm-diameter depression in the diaphragm. This caused in a small permanent change in membrane tension which might have been avoided by using a sintered metal plug or adhering a thin metal pad to the center of the diaphragm.

VI. RESULTS

The capacitance response of a pressure sensor with a 0.47-mm-thick silicon diaphragm is shown in Fig. 16. The center-point spacing s_0 was 72 μm. The sensor was evacuated which provided a static preload of 14.7-psi (101 kPa).

The OBPS pressure sensitivity is reasonably linear for capacitance changes up to 400%. A dynamic water column change of 0.10 mm (1.1 Pa) can be resolved at an ocean depth of 200 m (1.96 MPa), a pressure range of 125 dB for a signal bandwidth of 0.005–0.25 Hz. The response exhibits increasing sensitivity between 0 psi to 43.5 psi (0–0.3 MPa). This is attributed to not including gap capacitance C_G in the calculation of the electrode contour and possibly to a small error in form at its edge.

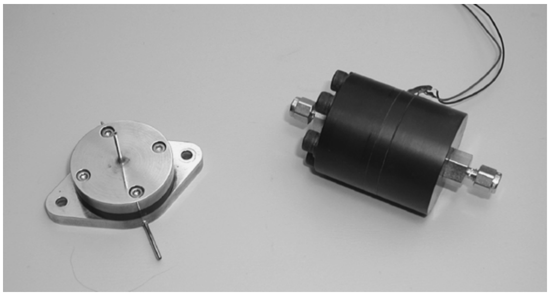

Fig. 15. Test fixtures for plastic transducers.

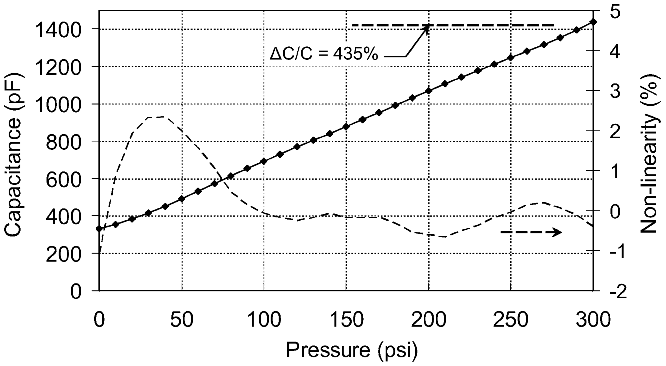

Fig. 16. Capacitance response of a pressure sensor with a 0.47-mm-thick silicon diaphragm.

The hysteresis of five sensors was measured by cycling the pressure calibrator up and down between 0–300 psi (0 and 2 MPa). A 0.1% to 0.3% increase in down pressure readings occurred midrange. The Psi-Tronix, PG5000 pressure gauge may have made a contribution to this difference.

The OBPS had a dynamic signal bandwidth of 0.005 to 0.25 Hz. Using a six-sigma conversion to obtain peak-to-peak noise, and accounting for equivalent noise bandwidths, the noise-floor of the electronics was 3.7 $\mu\mathrm{V}_{\mathrm{p-p}}$ when the electronics included an AD587 voltage reference. The noise of the reference below 0.25 Hz was reduced by about 6-dB by an RC low-pass filter. It employed a tantalum capacitor with a high dc working voltage that limited leakage current to pA levels. This method of filtering was possible for the OBPS because of the limited extremes of ocean temperature.

If resolution is defined as peak-to-peak signal to peak-to-peak noise, the AD587 noise limits the OBPS pressure resolution to 128 dB for a full-scale output range of 10 V. This value is in close agreement with typical measured values of 125 dB when the NBB operated at 200 KHz with a 10-V excitation voltage.

The sensitivity and dynamic range of a sensor with curved electrodes can be increased by using a thinner silicon diaphragm, but the increases are achieved at the expense of linearity, as shown in Fig. 17. For this sensor, with a 0.1-mm-thick silicon diaphragm, tensile stresses appear to dominate the response above 2.6 psi (18 kPa). The large capacitive change of 885% is unique to a transducer with a curved electrode.

The response of a pressure sensor with a 6-μm PC foil membrane is shown in Fig. 18. The contour and size of the rigid electrode are the same as those for sensors with silicon diaphragms; resources limited fabricating multiple templates. The response

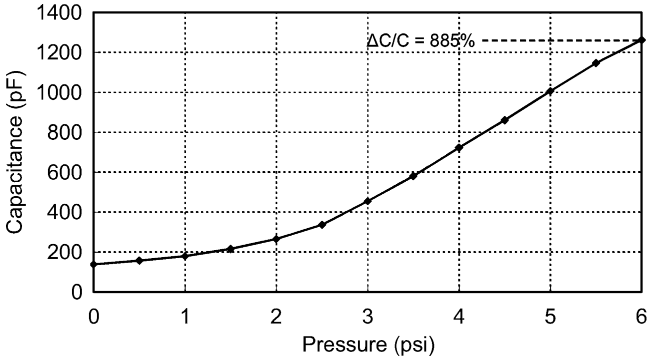

Fig. 17. Capacitance response of a pressure sensor with a 0.1-mm-thick silicon diaphragm.

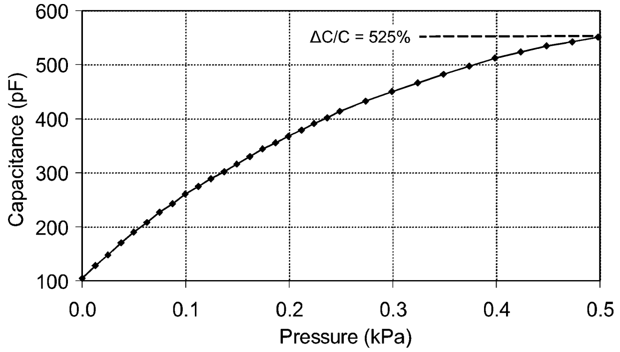

Fig. 18. Capacitance response of a pressure sensor with a 6-μm-thick PC membrane.

shows a decrease in sensitivity with pressure, the probable effect of a value of $n = 2.97$, instead of 2.0 in (11).

Fig. 19 shows the capacitance-voltage (C–V) response of a PC actuator with a 6-μm-thick membrane $(K_p \approx 36)$. The response has an approximate square-law voltage dependency up to about 20 V. An estimate of membrane displacement is shown on the second vertical axis.

The C–V response of an unevacuated silicon sensor with a 25-μm-thick diaphragm is shown in Fig. 20. Its capacitance increased from 188 pF at 0 V to 952 pF at 40 VDC. The response was unstable due to charging of the thin-film dielectric: a 1700-Å-thick layer of SiN deposed on a 1600-Å-thick layer of thermal oxide. Capacitance values observed at each higher value of applied voltage V_A drifted lower as the dielectric slowly accumulated charge.

Another C–V response (electret response) was obtained after 40 V was applied to the sensor for 15 min. The minimum (initial) value of capacitance (188 pF) was found at an applied voltage V_A of 18 V, indicating the formation of a temporary electret.

Electrets of equivalent magnitudes were formed with both positive and negative voltages that had relaxation time constants of several hours. The large polarization voltage V_E of the electret is attributed to the high field (120 V/μm) across the dielectric that caused charge trapping, charge accumulation at the thin-film interfaces, and surface charging of the nitride by ionized air.

The charging of the double layer dielectric shown in Fig. 20 is an extreme example, particularly since either layer alone would have provided adequate electrical insulation at low levels of mechanical stress.

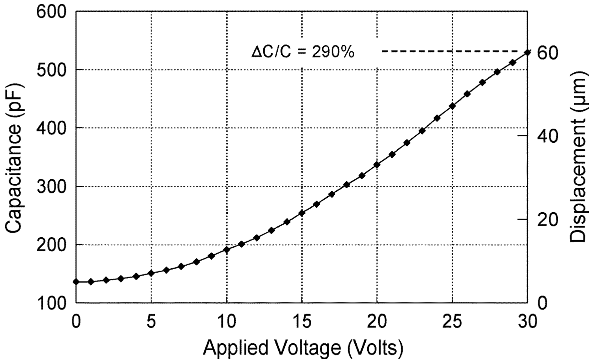

Fig. 19. C–V response of a PC actuator with a 6-μm-thick membrane.

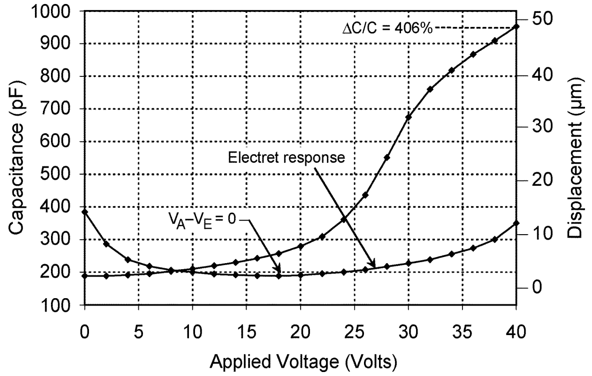

Fig. 20. C–V response of silicon actuator with 25-μm-thick silicon diaphragm.

For certain applications, e.g., acoustic projectors, it may be possible to utilize accumulated charge as an electret to mechanically preload a compliant electrode. For oxide or nitride films, the accumulated charge might be periodically refreshed. Electrets formed with polymer films appear to be more stable than those formed with crystalline films, but the potential across all dielectric films must remain well below the dielectric strength of the materials.

VII. OTHER DESIGNS AND APPLICATIONS

The performance and construction of capacitive pressure sensors were described in detail to demonstrate the advantages of transducers with contoured rigid electrodes. Other designs and applications are proposed here for future research.

A. Transducer Arrays

Transducer arrays can be constructed by bonding or suspending diaphragms over one-dimensional or two-dimensional arrays of circular or rectangular elements with curved electrodes [21]. The individual elements can be electrically connected in parallel or addressed individually. Fig. 21 illustrates a design concept for a 250-KHz linear phased array for a side-scanning sonar transducer having 2-mm wide × 25-mm long elements spaced 3-mm apart (half-wavelength spacing).

For a capacitor with a rectangular electrode of width w, contact width w_0, and length l, the contact capacitance C_C (in two

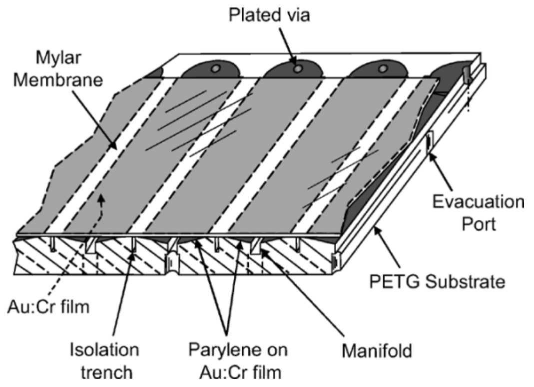

Fig. 21. Concept for side-scanning sonar transducer.

parallel strips) is $\varepsilon_a(w - w_0)l/t_d$. The gap capacitance C_G is obtained from (2) by changing C_p to $\varepsilon_0 w_0 l/s_0$.

The use of underwater electrostatic ultrasonic transducers has been restricted to calibration and measurements at shallow depths [22]. Hydrophones and projectors with curved rigid electrodes can operate at greater depths because the electrodes continuously control the collapse of a compliant electrode.

The high sensitivity of a transducer with a curved electrode can be traded-off to allow operation with a stiffer membrane to increased its electromechanical coupling coefficient to water. The stiffness of the transducer of Fig. 21 can also be increased by electrically connecting in parallel a group of narrower rectangular electrode elements.

For frequencies above 1 MHz, capacitive micromachined ultrasonic transducers (CMUTs) use silicon or SiN diaphragms because of the material's high elasticity and low intrinsic damping. Arrays of CMUTs have been fabricated for ultrasonic imaging applications in air and liquids [23]–[25]. They have an advantage in air over crystalline piezoelectric transducers because of a better acoustic impedance match to air and lower lateral-mode resonances. To minimize dielectric charging, it is desirable to evacuate the devices to allow operation at higher voltages.

B. MEM Transducers

Many applications appear to exist for MEM sensors and actuators with contoured electrodes. In addition to pressure and acoustic transducers, the possibility exists to fabricate arrays of micromirrors that are angularly controlled around one or two axes of tilt [26]. However, concerns arise about adhesion forces and stiction between the electrodes of actuators with microscale areas and spacings [27]. Cantilever beams adhere to smooth substrates due to Van der Wall forces, hydrogen bonding, and electrostatic forces.

Mechanical stiction from motion is a function of the surface roughness and the surface energy of opposing materials. It can be minimized by employing low-friction, low surface-energy dielectric films, e.g., Parylene, PVDF, and Teflon AF. Stick slip can also be reduced when capacitive detection electronics generate a periodic electrostatic force that continuously reseats a compliant electrode as it deflects.

Charge accumulation and its stability in organic and inorganic films limit the performance and applications for MEM actuators.

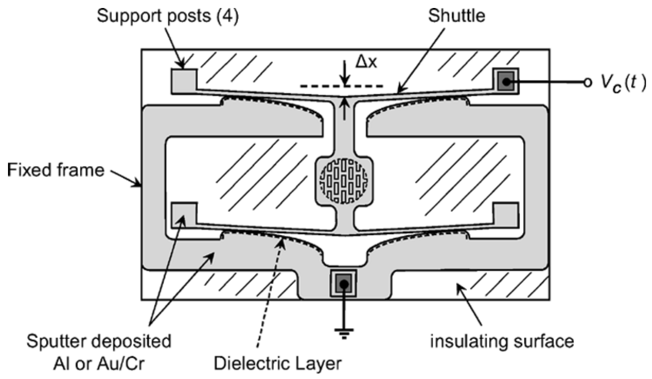

Fig. 22. Surface micromachined actuator with curved counter electrodes.

The force advantage (7) of a MEM actuator with a thin film dielectric cannot be fully realized with high permittivity films. The field strength in ceramic dielectrics, e.g., $\mathrm{Si_xNi_y}$ strongly influence charge buildup in the film [28]. This limits control voltages to values well below the breakdown voltage of a capacitive transducer.

C. Surface Micromachined Transducers

Bulk dissolved silicon processing and deep ion etching of single and polycrystalline silicon are used to fabricate MEM accelerators with comb electrodes [29]–[32]. These methods appear capable of fabricating electrostatic actuators (engines) that provide large forces compared to actuators with parallel electrodes. Fig. 22 shows a concept for an actuator with four, forcer elements to which additional elements can be added.

The etch-released shuttle can include an inertial mass for sensing acceleration. Its sensitivity may be less than accelerometers with comb electrodes of variable or fixed spacing. The quality factor Q_c of an accelerator with electrodes in partial contact is reduced by the hysteresis of interfacial slip: the difference between adhesion energy between the extension and contraction of the area of electrode contact. A conventional accelerometer has a sensitivity advantage when its value of Q is greater than $2K_pQ_c$. However, an accelerator with curved electrodes operating with a NBB offers advantages to active damping systems used to control low-frequency vibration.

D. Actuators Controlled by Force-Balanced Feedback

The deflection of an electrode can be controlled by force-balanced feedback. A conceptual example is illustrated in Fig. 23: a beam steering mirror that is bi-directionally rotated by tractive forces applied by two capacitors, $C_1(\theta)$ and $C_2(\theta)$.

The mirror is supported along its axis of rotation by a pair of torsional flexures. Two, free-standing dielectric films, each with a hinged section, are connected to the optical element and to the outer edge of the rigid electrodes of $C_1(\theta)$ and $C_2(\theta)$. A metal layer is deposited on the dielectric members to form compliant electrodes. An optional convex bearing surface (not shown) can be placed under the mirror to further constrain vertical displacement.

The capacitance difference between the two actuators can be measured using the NBB of Fig. 8, when reference capacitor

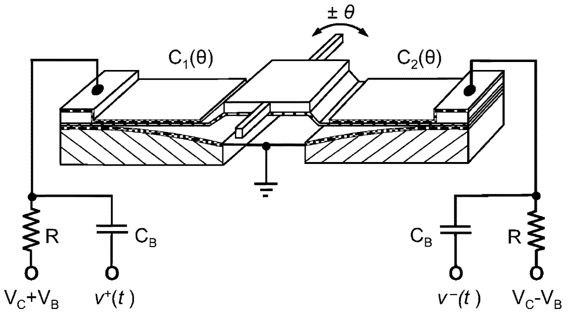

Fig. 23. Differential transducer with curved electrodes that senses and controls the angular position of an optical element.

C_R is replaced by a second variable capacitor. Bridge excitation pulses of frequency ω are applied to the actuators through FET switches and blocking capacitors C_B. Since C_B is large compared to $C_1(\theta)$ and $C_2(\theta)$, the voltages $v^+(t)$ and $v^-(t)$ at the inputs to C_B (bridge outputs) are identical to the waveforms of Fig. 9. A differential bias voltage $\pm V_B$ is applied across resistors R, when $(R \gg 1/\omega C_B)$. The bias voltages $\pm V_B$ provide a balanced torque to opposing sides of the mirror.

The energy W_e stored by $C_1(\theta)$ or $C_2(\theta)$ can be expressed as

$$W_e = \frac{1}{2} C(\theta) V^2 \tag{14}$$

where θ is the angle of rotation of the element, and V the voltage applied across the capacitor electrodes. The electrostatic torque F_e arising from a change in energy W_e due to a change in angle θ is

$$F_e = \frac{\partial W_e}{\partial \theta} = \frac{1}{2} \frac{\partial C(\theta)}{\partial \theta} V^2. \tag{15}$$

For an applied bias $\pm \mathrm{V_B}$, the mirror resides at its neutral position $\theta = \theta_0$ and capacitors $C_1(\theta)$ and $C_2(\theta)$ are substantially equal. A position control voltage $V_C < |V_B|$ is superimposed on the bias voltages to create a tractive force to rotate the mirror to a new angle θ_i for force-balanced equilibrium. The net force F of the system at this position of torque equilibrium can be expressed as

$$F(\theta_i) = \frac{\partial C_1(\theta)}{\partial \theta} \frac{(V_C + V_B)^2}{2} - \frac{\partial C_2 \theta}{\partial \theta} \frac{(V_C - V_B)^2}{2} - k_\theta \theta \tag{16}$$

where k_θ is the torsional spring constant of the support beams. It is assumed k_θ is linear for $\theta_i \leq$ a maximum angle $\theta_{\max}$ and the electrode contour maintains $\partial C(\theta)/\partial \theta$ at a substantially constant value k_1 for tilt angles $\leq |\theta_{\max}|$. For these conditions, (16) yields

$$F(\theta_i) = 2 k_1 V_B V_C - k_\theta \theta. \tag{17}$$

Equation (17) indicates the angle of tilt θ has a linear response with control voltage V_C. The gain G_D of this electric-field coupled system, found by differentiation, is

$$G_D = \frac{dF}{dV_C} = 2 k_1 V_B \quad (\theta_i \leq |\theta_{\max}|) \tag{18}$$

that indicates G_D is proportional to V_B. Accordingly, the open-loop gain and voltage-angle response of the transducer are largely independent of angular deflection.

The actuator concept of Fig. 23 is feasible if the accumulation of charge by the free-standing dielectric film is stable, or if it can be periodically refreshed. This would require periodically deflecting the movable electrode over its full range of travel with a voltage exceeding values of V_C used for control. A stable charge forms an electret that provides a bias potential of equal polarity across each capacitor. When this is the case, a differential control voltage $\pm V_C$ is used to rotate the mirror.

E. Electret Transducers

When a dielectric layer becomes permanently electrically polarized, it becomes an electret. The effective polarization voltage of electret microphones can be as high as 200 V. The voltage V developed across the dielectric is proportional to the film thickness t_d and its effective charge density ρ, where $V = \rho t_d / \varepsilon_a$. The charge density of an electret of a transducer with a curved electrode can be lower because of the small electrode spacing maintained by the dielectric layer.

Electrets provide a low-noise potential to electrically self-bias sensors and mechanically bias actuators [33]. An early method to form electrets for microphones is described by Sessler and West [34]. A thermoplastic film is heated above its glass transition temperature and then cooled in a strong electric field. Electrets are also be formed by the direct implantation of electrons or ions in dielectric films [35].

Stable electrets can be formed from fluoropolymer and high-performance polymer films that are suitable for constructing transducers with curved electrodes, e.g., PET, parylene, and Teflon AF. Methods also have been claimed for forming stable electrets in $\mathrm{SiO_2}$. They involve heating the material before implantation [36]. It appears it would also be advantageous to preheat the film in vacuum and to anneal it after implantation to further enhance charge stability.

A method of Yasuno and Riko is of special interest [37]. Ions or electrons are implanted through a thin metal film of a capacitor electrode into a supporting dielectric layer. The buried charge is isolated from surface dynamics and environments. This method appears practical to form electrets in devices of complex construction, e.g., CMUT arrays and the tilt mirror of Fig. 14.

VIII. CONCLUSION

Capacitive transducers with curved electrodes have advantages over capacitive sensors and actuators with parallel electrodes for many potential applications. The capacitive sensitivity of a transducer with curved electrodes can be two or three orders of magnitude greater than that of a conventional transducer of comparable size. The form of a rigid electrode can be selected to provide a linear capacitive response over a wide dynamic range. It continuously mechanically controls the deflection of a compliant electrode to avoid electrostatic collapse. The precise shape of the rigid capacitor electrode is not critical for microphones, accelerometers, and ultrasonic transducers that have small membrane displacements around a mechanically fixed or electrically biased operating point.

The sensitivity and force exerted by transducers with curved electrodes can be characterized by a figure-of-merit K_p, a product of relative electrical and mechanical advantages. Pressure sensors with a stiff silicon diaphragm resolved dynamic pressure changes over a substantially linear dynamic range of 125 dB. This range was limited by the noise of a precision voltage reference. Capacitive changes of 885% were obtained for a sensor with a thin silicon diaphragm.

A new measurement circuit was developed to accommodate the very large capacitance changes of capacitors with contoured electrodes. The circuit, that allows one capacitor electrode to be grounded, includes an active capacitive bridge nulled by current feedback. It also can be used to detect the deflection of the compliant electrode of an actuator to provide a signal for force-balanced feedback.

Capacitive transducers with curved electrodes appear well suited for MEMS applications, but the performance of MEMS actuators is limited by the accumulation and trapping of charge in thin dielectric films.

APPENDIX

A. Calculation of Variable Gap Capacitance

An estimate is made here of the gap capacitance C_G of a capacitor with a contoured electrode using the linear model of Fig. 4. The capacitance includes two serial components: C_a with a fixed dielectric layer of permittivity ε_a and C_b with a variable gap of permittivity ε_0. The gap capacitance can be expressed as

$$C_G = \int_0^{r_0} \frac{dC_a dC_b}{dC_a + dC_b}. \tag{A1}$$

Capacitances dC_a and dC_b are

$$dC_a = \frac{\varepsilon_a \pi r}{t_d} dr; \quad dC_b = \frac{\varepsilon_0 \pi r}{s'} dr \quad (0 \le r \le r_0) \tag{A2}$$

where the electrode spacing $s' = s_0(r_0 - r)/r_0$ at radius r. The incremental gap capacitance can be written as

$$dC_G = \frac{\varepsilon_a \varepsilon_0 \pi}{\varepsilon_a s' + \varepsilon_0 t_d} r dr. \tag{A3}$$

Substituting for s' in (A3) and rearranging terms provides

$$dC_G = \frac{K r dr}{r_0(\varepsilon_a s_0 + \varepsilon_0 t_d) - \varepsilon_a s_0 r} \tag{A4}$$

where $K = \pi \varepsilon_a \varepsilon_0 r_0$.

To prepare (A4) for integration, let $a = r_o(\varepsilon_a s_0 + \varepsilon_0 t_d)$ and $b = -\varepsilon_a s_0$. Capacitance C_G can now be expressed as

$$C_G = K \int_0^{r_0} \frac{r dr}{a + br}. \tag{A5}$$

After integration and arranging terms

$$C_G = K \frac{a}{b^2} \left[ln \left(\frac{a}{a + br_0} \right) + \frac{b}{a} r_0 \right]. \tag{A6}$$

From the assignments of K, a, and b, the following expressions are obtained for terms Ka/b^2, $a/(a + br_0)$, and br_0/a in (A6).

1) The first term

$$\frac{Ka}{b^2} = \frac{\varepsilon_a \varepsilon_0 \pi r_0^2 (\varepsilon_0 t_d + \varepsilon_a s_0)}{\varepsilon_a^2 s_0^2} = C_P \beta \tag{A7}$$

where $C_P = \varepsilon_0 \pi r_0^2 / s_0$ is the capacitance of a parallel-plate capacitor with electrodes of radius r_0 and spacing s_0, and

$$\beta = \frac{\varepsilon_0 t_d + \varepsilon_a s_0}{\varepsilon_a s_0} = \frac{1}{K_p} + 1 \tag{A8}$$

where K_p is the figure of merit identified earlier in (6).

2) The second term becomes

$$\frac{a}{a + br_0} = \frac{\varepsilon_a s_0 + \varepsilon_0 t_d}{\varepsilon_0 t_d} = K_p + 1. \tag{A9}$$

3) The third term is

$$\frac{b}{a} r_0 = \frac{-\varepsilon_a s_0}{(\varepsilon_a s_0 + \varepsilon_0 t_d)} = -\frac{1}{\beta}. \tag{A10}$$

Equation (A6) can be now written as

$$C_G = C_P \beta \left[\ln(K_p + 1) - \frac{1}{\beta} \right]. \tag{A11}$$

Values of K_p from Table I for silicon and PC sensors provide values of $\beta = 1/K_p + 1$ of 1.001 and 1.014, respectively, which justifies the following approximation:

$$C_G \approx C_P \left[\ln(K_p + 1) - 1 \right]. \tag{A12}$$

B. Electrode Contour for a Membrane Electrode

This analysis determines the form of the rigid electrode for a capacitor with a membrane electrode that provides a linear increase in capacitance with applied pressure. It is based on three assumptions: 1) a change in tension ΔT caused by membrane displacement is negligible compared to the initial value of assembled tension T, 2) membrane deflection is determined only by reactive tensile stresses, and 3) contact capacitance C_C is large compared to gap capacitance C_G.

The form of the free surface of the membrane is governed by the equilibrium equation

$$T \nabla^2 z = p \tag{A13}$$

where z is membrane deflection and p is the normal pressure at the surface of the membrane. For a radially symmetric system, (A13) has the solution

$$z = \frac{p}{4T} r^2 \quad (0 \le r \le R). \tag{A14}$$

Continuity at the radius $r(p)$ of the boundary of electrode contact requires the slope of the contour and the edge slope of the free-standing membrane be equal. For this constraint, the supporting contour must obey the equation

$$\frac{\partial z}{\partial r} = \frac{pr(p)}{2T}. \tag{A15}$$

For a linear response, (10) requires that the annular area of electrode contact be a linear function of pressure. Solving (10) for p and substituting into (A15) yields a first-order differential equation for the supporting contour

$$\frac{dz}{dr} = \frac{(R^2 - r^2)r}{4\xi T} \tag{A16}$$

that has a solution

$$z = \frac{r^2}{4\xi T}\left(R^2 - \frac{r^2}{2}\right) + K. \tag{A17}$$

The integration constant K is chosen so that $z(R)$ is zero at the contact boundary (beginning of contour). Factoring terms and normalizing to R yields

$$z = -\left(\frac{R^4}{8\xi T}\right)(1 - \rho^2)^2 \tag{A18}$$

where $\rho = r/R$. For design, it is convenient to express (A18) in terms of maximum pressure $p_{\max}$ at contact radius $r_0 = 0$. Solving (10) for $p_{\max}$ and substituting into (A18) yields

$$z = -\left(\frac{R^2 p_{\max}}{8T}\right)(1 - \rho^2)^2. \tag{A19}$$

Given the explicit form of the supporting contour in (A19), it can determined to what extent the first assumption (constant tension) is valid. If the membrane is of a linearly elastic material, the change in tension with membrane deflection will be proportional to the change in strain. The strain may be determined from the difference between the arc length along a radial path over the supporting contour and the radial coordinate of that path. The arc length is given by

$$\frac{ds}{dr} = \sqrt{1 - \left(\frac{dz}{dr}\right)^2} \tag{A20}$$

and the strain by

$$\frac{d\varepsilon}{dr} = \sqrt{1 - \left(\frac{dz}{dr}\right)^2} - 1 \approx \frac{1}{2}\left(\frac{dz}{dr}\right)^2. \tag{A21}$$

In this case, the first-order Taylor series approximation to the square root is valid for strains that are sufficiently small to meet the constant-strain assumption of the basic calculation. The maximum strain $\varepsilon_{\max}$ is found by integrating across the radius. Upon substitution of (A19) into (A21) the maximum strain is

$$\begin{aligned} \varepsilon_{\max} &= \left(\frac{r_0 p_{\max}}{16T}\right)\int_0^1 \left(\frac{d}{d\rho}(1 - \rho^2)^2\right)^2 d\rho \\ &= \frac{128}{105} \cdot \frac{r_0 p_{\max}}{16T} \approx \frac{r_0 p_{\max}}{13T}. \end{aligned} \tag{A22}$$

The pretension T is a function of the initial assembly strain ε_T, the thickness of the membrane t, and the elastic modulus of the membrane material E

$$T = Et\varepsilon_T. \tag{A23}$$

One may, thus, express both the contour depth and the figure of merit for the constant tension assumption as a function of the membrane properties and initial strain

$$z_{\max} = -\frac{r_0^2 p_{\max}}{8Et\varepsilon_T} \tag{A24}$$

$$\frac{\varepsilon_{\max}}{\varepsilon_T} \approx \frac{r_0 p_{\max}}{13Et\varepsilon_T^2}. \tag{A25}$$

Alternatively

$$\varepsilon_{\max} \approx \frac{8}{13} \cdot \frac{z_{\max}}{r_o}. \tag{A26}$$

As expected, the change in tension is least in shallow contours which result from relatively large pretension. Sensor designs for which the variation in tension is unacceptably large may be modified by using the tension predicted from (A21) to modify the tension in (A15) and resolve for the contour. This process can be continued iteratively until arbitrary theoretical accuracy is obtained.

ACKNOWLEDGMENT

The authors would like to thank V. S. Newton, former Branch Chief, Naval Surface Warfare Center, White Oak, MD, for his long-term encouragement and support. They would also like to thank Winfield Hill, Director of Electronics, Rowland Institute at Harvard, for assistance in developing the null-balanced capacitive bridge.

REFERENCES

[1] B. C. Carter, J. F. Shannon, and J. R. Forshaw, “Measurement of displacement and strain by capacity methods,” *Proc. J. Mech. Eng.*, vol. 152, pp. 215–221, 1945.

[2] E. Frank, *Electrical Measurement Analysis*. New York: McGraw-Hill, 1959, pp. 373–374.

[3] M. Slavin, R. W. Carp, and G. T. Bata, “Pressure variable capacitor,” U.S. Patent 3 993 939, Nov. 23, 1976.

[4] D. J. Young, J. Du, C. A. Zorman, and W. H. Ko, “High-temperature single-crystal 3C-SiC capacitive pressure sensor,” *IEEE Sensors J.*, vol. 4, no. 4, pp. 464–470, Aug. 2004.

[5] W. H. Basarab-Horwath and B. E. Jones, “A capacitor transducer using a thin dielectric and variable-area electrode,” *Proc. Inst. Elect. Eng. A*, vol. 127, no. 6, pp. 392–394, 1980.

[6] NIST Division Test Rep., 822.01/8220592, S56, May 5, 1992.

[7] B. Block, “Capacitive force transducer,” U.S. Patent 4 225 755, Sep. 30, 1980.

[8] R. B. McIntosh, P. E. Mauger, and S. R. Patterson, “Wide Dynamic range capacitive transducer,” U.S. Patent 6 151 967, Nov. 28, 2000.

[9] S. R. Legtenberg *et al.*, “Electrostatic curved electrode actuators,” *J. Microelectromech. Syst.*, vol. 6, no. 3, pp. 257–265, Sep. 1997.

[10] R. B. McIntosh, “Method to force-balance capacitive transducers,” U.S. Patent 6 496 348, Dec. 17, 2002.

[11] D. Huber, P. Corredoura, S. Lester, V. Robbins, and L. Kamas, “Reducing Brownian motion in an electrostatically tunable MEMS laser,” *J. Microelectromech. Syst.*, vol. 13, no. 4, pp. 732–736, Dec. 2004.

[12] J. Drake and H. Jerman, “A micromachined torsional mirror for track following in magneto-optical drives,” in *Proc. Solid-State Sensor and Actuator Workshop*, Hilton Head, SC, 2000, pp. 10–13.

[13] Parylene Specifications and Properties, Speedline Technologies-Specialty Coating Systems, Indianapolis, IN, 2000.

[14] T. J. Yao, K. Walsh, and Y. C. Tai, "Dielectric charging effects on parylene electrostatic actuators," in *Proc. IEEE Int. Conf. Microelectrmechanical Systems*, Las Vegas, NV, 2002, pp. 614–617.

[15] H. L. Chau and K. D. Wise, "Noise due to Brownian motion in ultrasensitive solid-state pressure sensors," *IEEE Trans. Electron Devices*, vol. ED-34, no. 4, pp. 859–865, Apr. 1987.

[16] T. B. Gabrielson, "Mechanical-thermal noise in micromachined acoustic and vibration sensors," *IEEE Trans. Electron Devices*, vol. 40, no. 5, pp. 903–909, May 1993.

[17] R. B. McIntosh and W. Hill, "Linear capacitance detection circuit," U.S. Patent 6 456 477, Sep. 24, 2002.

[18] L. Smith and D. H. Sheingold, Noise and Operational Amplifier Circuits, Analog Devices, Norwood, MA, 1993.

[19] P. Linder, T. Glinsner, and C. Schaefer, "One micron precision optically aligned method for hot-embossing and nanoimprinting," *Proc. IEEE Sensors*, vol. 2, pp. 931–935, 2002.

[20] PPS Film Torelina Mechanical Properties. [Online]. Available: www.toray-int.jp

[21] R. B. McIntosh, P. E. Mauger, and S. R. Patterson, "Method to construct variable-area capacitive transducers," U.S. Patent 6 556 417, Apr. 29, 2003.

[22] W. Yost and J. Cantrell, "Absolute ultrasonic displacement measurements with a submersible electrostatic acoustic transducer," *Rev. Sci. Instrum.*, vol. 63, no. 9, pp. 4182–4188, Sep. 1992.

[23] I. Ladabaum, X. Jin, H. T. Soh, A. Atlar, and T. Khuri-Yakub, "Ca-pacitive micromachined ultrasonic transducers," *IEEE Trans. Ultrason., Ferroelect., Freq. Control*, vol. 45, no. 3, pp. 678–690, Mar. 1998.

[24] I. Oppenheim, A. Jain, and D. W. Greve, "Electrical characterization of coupled and uncoupled MEMS ultrasonic transducers," *IEEE Trans. Ultrson., Ferroelect., Freq. Control*, vol. 50, no. 3, pp. 207–304, Mar. 2003.

[25] B. T. Khuri-Yakub *et al.*, "Capacitive micromachined ultrasonic transducers: next-generation arrays for acoustic imaging," *IEEE Trans. Ultrson., Ferroelect., Freq. Control*, vol. 49, no. 11, pp. 1596–1610, Nov. 2002.

[26] R. B. McIntosh and S. R. Patterson, "Apparatus and method to angularly position micro-optical elements," U.S. Patent 6 661 637, Dec. 9, 2003.

[27] J. A. Knapp and M. P. de Boer, "Mechanics of microcantililever beams subject to combined electrostatic and adhesive forces," *IEEE J. Microelectromech. Syst.*, vol. 11, no. 6, pp. 754–764, Jun. 2002.

[28] E. K. Chan, K. Garikipati, and R. W. Dutton, "Characterization of contact electromechanics through capacitance-voltage measurements and simulations," *IEEE J. Microelectromech. Syst.*, vol. 8, no. 2, pp. 208–217, Feb. 1999.

[29] S. J. Sherman, R. W. K. Tsang, and T. Core, "Monolithic accelerometer," U.S. Patent 5 540 095, Jul. 30, 1996.

[30] Y. Gianchandani and K. Najafi, "A bulk silicon dissolved wafer process for micromechanical systems," *IEEE J. Microelectromech. Syst.*, vol. 1, no. 2, pp. 77–85, Feb. 2002.

[31] G. J. Galvin, T. J. Davis, and N. C. MacDonald, "Micromechanical accelerometer for automobile applications," U.S. Patent 6 149 190, Nov. 21, 2000.

[32] K. H. Han and Y. H. Cho, "Self-balanced navigation-grade capacitive microaccelerometers using branched finger electrodes and their performance for varying sense voltage and pressure," *IEEE J. Microelectromech. Syst.*, vol. 12, no. 1, pp. 11–20, Jan. 2003.

[33] R. B. McIntosh, "Electret transducer," U.S. Patent 6 658 938, Dec. 9, 2003.

[34] G. M. Sessler and J. E. West, "Self-biased condenser microphone with high capacitance," *J. Acoustic. Soc. Amer.*, vol. 34, pp. 1787–1788, 1962.

[35] W. H. Hsieh, T. Y. Hsu, and Y. C. Tai, "A micromachined thin-film Teflon electret microphone," in *Proc. Tech. Dig., Int. Conf. Solid State Sensors and Actuators*, vol. 1, 1997, pp. 425–428.

[36] J. Lewiner and D. Pernio, "SiO_2 Electrets and process of making it," U.S. Patent 5 486 423, Jun. 23, 1996.

[37] D. Yasuno and Y. Riko, "Condenser microphone and production method thereof," U.S. Patent 6 731 776, May 4, 2004.

Robert B. McIntosh (SM'88) received the B.S. degree in electrical engineering from the University of Pennsylvania, Philadelphia, in 1961 and the M.S. degree in electrical engineering from New York University in 1962.

He founded Horizon Technology Group, Inc., in 1986 and was President until his retirement in 2004. Earlier, he was with the Microlithography Group and Optical Group of Perkin-Elmer Corporation, Norwalk, CT.

Philip E. Mauger received the B.S. degree in physics and mathematics from Drew University, Madison, NJ, in 1975 and the M.S. and Ph.D. degrees in physics from Cornell University, Ithaca, NY, in 1982.

He is Vice President of Nanostructures, Inc., Santa Clara, CA, a company he cofounded in 1987. Earlier, he developed processing technology for X-ray masks at Micronix Corporation and for thin-film products at Source Technology, Inc., and Watkins-Johnson Corporation.

Steven R. Patterson received the B.S. degree in physics from the California Institute of Technology, Pasadena, in 1970 and the M.S. and Ph.D degrees in mechanical engineering from the University of California at Davis in 1987.

He is the SPX Distinguished Professor of precision engineering at the University of North Carolina at Charlotte. Earlier, he served in a variety of positions at the Lawrence Livermore National Laboratory, Livermore, CA.